https://doi.org/10.1016/j.actamat.2020.02.039

Achieving exceptional wear resistance in a compositionally complex alloy via tuning the interfacial structure and chemistry

Weiwei Zhu[a,b], Cancan Zhao[a], Yiwen Zhang[a], Chi Tat Kwok[b,c], Junhua Luan[d], Zengbao Jiao[e], Fuzeng Ren[a,*]

[a] Department of Materials Science and Engineering, Southern University of Science and Technology, Shenzhen, Guangdong 518055, China

[b] Institute of Applied Physics and Materials Engineering, Faculty of Science & Technology, University of Macau, Macau, China

[c] Department of Electromechanical Engineering, Faculty of Science and Technology, University of Macau, acau, China

[d] Center for Advanced Structural Materials, Department of Materials Science and Engineering, City University of Hong Kong, Hong Kong, China

[e] Department of Mechanical Engineering, The Hong Kong Polytechnic University, Hong Kong, China

Abstract

Titanium alloys have been widely used for medical devices and structural applications. However, conventional titanium alloys often suffer from low resistance to wear, particularly at elevated temperatures. Herein, an equiatomic TiMoNb compositionally complex alloy (CCA) is shown to exhibit wear resistance comparable to alumina at room temperature (RT). Even at 600℃, the alloy still shows an extremely low wear rate of the order of $10^{-6} mm^3/(N-m)$. The remarkable wear resistance is achieved via tuning the interfacial structure and chemistry in TiMoNb CCA, including nanostructuring, titanium segregation at the grain boundaries, and the formation of a high density of nanoscale coherent Ti-rich precipitates with cube-on-cube orientation relationship with the ultrafine-grained matrix. The present results provide significant insights into the design of novel alloys for service in harsh environments.

1. Introduction

Sliding wear is a key factor that limits the lifetime of metallic components for a wide range of functional and structural applications[1]. Thus, the design of novel metallic alloys with exceptional wear resistance is in great demand for ensuring the reliability, durability, and efficiency of metallic contacts in harsh environments[2,3]. During sliding of the metallic components at room or lower temperature, the material's hardness and sliding-induced microstructure evolution below the sliding surface have been linked to wear resistance[2 8]. In contrast, at elevated temperatures, the surfaces are not only subjected to the stress associated with frictional and contact forces, but also susceptible to thermal softening and oxidation by reaction with oxygen, which may significantly change the overall wear performance[9]. Such a complex mechanical and thermal environment interplay requires dedicated design of the grain structure of metallic alloys that can maintain high stability during wear at elevated temperatures.

Titanium alloys have demonstrated high strength, extraordinary corrosion resistance, and the ability to withstand extreme temperatures. These remarkable properties enable titanium alloys a variety of applications, ranging from medical devices, such as orthopedic, dental and prosthetic implants, to many other engineering components in industrial, automotive, and aerospace fields[4]. However, the conventional titanium alloys suffer from a major drawback: poor wear resistance[10,11], with the wear rates usually in the order of $10^{-6}-10^{-3} mm^3/(Nm)$ upon sliding against alumina[12], which limits their widespread use in harsh environments. In the biomedical field, for example, low wear resistance-induced implant loosening and the generated wear particles-induced inflammatory response of orthopedic titanium alloys are the main concerns of total joint replacement arthroplasty[13,14]. Thus, improving the wear characteristics at room and elevated temperatures is of prime importance for the in-

service longevity of titanium alloys. Since wear resistance empirically correlates with material's hardness, two common strategies have been used to improve the wear resistance of titanium alloys through enhanced hardness: (i) alloying via solute drag to retard motion of grain boundaries (GBs) or Zener pinning through formation of second-phase precipitates/particles[15] and (ii) grain size reduction by introducing a large volume fraction of GBs[16,17]. However, the first strategy can only result in modest increase in wear resistance and if the secondphase precipitate/particle-matrix interfaces are incoherent, they may even facilitate crack nucleation under cyclic loading due to weak interface bonding, and thus lead to decreased fatigue wear resistance[18]. Moreover, the efficacy of the second strategy often diminishes at elevated temperatures due to grain growth[19].

To increase the thermo-mechanical stability of ultrafine-grained (UFG) or nanostructured alloys, tuning the interfacial structure and chemistry via preferential segregation of solute atoms to GBs to reduce the boundary energy, and thus the driving force for grain growth, offers a promising thermodynamic approach[20-23]. For example, by modifying GB energies via solute segregation, ultralow wear has been recently achieved in nanocrystalline Pt-Au thin films[3]. Using the strategy of combined nanostructuring and complexion engineering, the tradeoff between strength and ductility can be avoided[24,25] and extreme thermal stability[26] can be achieved in Cu-based alloys. However, to date, complexion engineering has been studied and utilized predominantly in the conventional binary alloys with one principal element, in the form of either coarsegrained/nanostructured alloys or bicrystals[24,27], but has never been reported in high-entropy alloys (HEAs) or compositionally complex alloys (CCAs) with multi-principal elements. HEAs/CCAs have demonstrated attractive properties that are not attainable in conventional alloys[28 33]. The intrinsic solid solution hardening and the sluggish diffusion effect in HEAs/CCAs make the design and use of complexion engineering more challenging.

On the other hand, engineering coherent internal boundaries at the nanoscale can also offer additional strengthening or hardening effect on the matrix[34], and thus further enhance the material's resistance to wear.

Herein, we present a design strategy through a combination of nanostructuring, complexion engineering, and the formation of a high density of coherent nanoscale precipitates at the GBs, to achieve exceptional wear resistance of a CCA both at room and elevated tempera- tures. As a proof of concept, we select equiatomic TiMoNb alloy as our model system. The reasons are five-folds: (i) the three binary equilibrium phase diagrams (Ti-Mo[35], Ti-Nb[36], Mo-Nb[37]) show that a minor amount of Ti would precipitate from the body-centered cubic (bcc) solid solution during cooling, while Mo and Nb are completely miscible; (ii) the three constituent elements have very close atomic radii ($r_{\mathrm{Ti}} = 1.46\text{Å}, r_{\mathrm{Mo}} = 1.36\text{Å}$ and $r_{\mathrm{Nb}} = 1.43\text{Å}$), facilitating the formation of coherent precipitates; (iii) the alloy contains relatively lighter elements than those found in the refractory HEA/CCA family (e.g. Hf, W, and Ta), thereby providing a lightweight refractory alloy; (iv) the three elements are biocompatible[38] and have high resistance to corrosion[39], enabling the obtained alloy suitable for orthopedic, dental and prosthetic applications[4]; and (v) Mo and Nb are beta-titanium stabilizing elements and can also increase the oxidation resistance of titanium alloys at high temperatures[40]. We have fabricated the equiatomic TiMoNb alloy by mechanical alloying followed by consoli- dation via spark plasma sintering (SPS). The mechanical alloying with a high-energy ball milling forces the elemental powders to form a nano- structured solid solution phase and the fast cooling during SPS induces the solute atoms segregation and the formation of a high density of nanoscale coherent precipitates at the GBs of the UFG matrix. This particular microstructure results in exceptional wear resistance both at room and elevated temperatures.

2. Experimental

2.1. Materials and fabrication

TiMoNb bulk alloy was prepared from high-purity Ti (99.5%, »325 mesh, Alfa Aesar, Ward Hill, Massachusetts, USA), Mo (99.9%, 1—5μm, Sigma-Aldrich, Darmstadt, Germany), and Nb powders (99.8%,1—5μm, Alfa Aesar, Ward Hill, Massachusetts, USA) by mechanical alloying and SPS. The powder mixture of Ti, Mo, and Nb with equia- tomic ratio and hardened steel balls were loaded into a hardened steel vial at a ball-to-powder weight ratio of 5:1 and subjected to high-energy ball milling using a SPEX 8000D (SPEX SamplePrep LLC, Metuchen, New Jersey, USA) mill at room temperature (RT) in an argon glove box for 12h. Considering the three binary phase diagrams of Ti-Mo[35], Ti-Nb[36], Mo-Nb[37] all show the formation of bcc phase at 900℃ and referring to the only available two isother- mal sections (at 1100℃ and 600℃) of the phase diagram of Ti-Mo-Nb ternary alloy[41], the 12h-milled powders were consolidated by SPS (SPS-211Lx, Fujidempa Kogyo. Co., Ltd., Osaka, Japan) at 900℃ under a pressure of 45MPa in vacuum. Specimens for subsequent characterization and tests were sectioned by electrical discharge machining from the as-fabricated cylindrical alloy.

2.2 Microstructure characterization

The phases of the ball-milled powders, compacted bulk samples, and wear debris were identified by X-ray diffraction (XRD) analysis performed on a Rigaku Smartlab-9kW (Rigaku, Tokyo, Japan) diffractometer in the 2θ range of 20—90° using Cu-Kα radiation (λ=1.54Å，45 kV, 200 mA). The grain size of the as-fabricated alloy was measured by electron backscatter diffraction (EBSD) (Nordlys Max^2, Oxford Instruments plc, Oxford, UK). The microstructure of the as-fabricated alloy and the ND-

SD (normal direction-sliding direction) cross-sections below the sliding surface from the wear tracks were analyzed by transimissiom electron mocscopy (TEM), high resolution TEM (HRTEM), and high-angle annular dark-field scanning transmission electron microscopy (HAADF-STEM) coupled with energy-dispersive X-ray spectroscopy (EDS) on an FEI Tecnai F30 TEM microscope operating at 300kV and an FEI Talos F200X TEM operated at 200kV (FEI Technologies Inc, Hillsboro, Oregon, USA). The TEM samples were prepared by focused ion beam (FIB: Helios Nanolab^{TM} 600i, FEI Technologies Inc, Hillsboro, Oregon, USA) using the site-specific, standard lift-out technique. The morphology and chemical composition of the wear tracks and wear debris were examined using a scanning electron microscope (SEM; MIRA 3, TESCAN, Czech Republic) equipped with an EDS detector.

2.3. Composition characterization

The three-dimensional (3D) composition of the as-fabricated TiM-oNb alloy was characterized using atom probe tomography (APT). Needle-shaped specimens were fabricated by lift-outs and annular milled in a FEI Scios FIB/SEM. The APT characterization was performed in a local electrode atom probe (CAMEACA LEAP 5000 XR). The specimens were analyzed at 50 K in voltage mode, a pulse repetition rate of 200 kHz, a pulse fraction of 20%, and an evaporation detection rate of 0.5% atom per pulse. Integrated Visualization and Analysis Software (IVAS) version 3.8 was used for creating the 3D reconstructions and data analysis.

The surface composition of the wear tracks was also analyzed by X-ray photoelectron spectroscopy (XPS; Thermo Scientific K-alpha, Thermo Fisher Scientific, UK) with a monochromatic Al $K\alpha$ source.

2.4 Density and hardness measurements

The density of the as-fabricated alloy was measured via Archimedes method (ASTM B962-15). Vickers micro-hardness at RT was measured using a Vickers diamond pyramidal indenter (HXD-1000TMC/LCD, Shanghai Taiming Optical Instrument Co., Ltd., Shanghai, China) under a 500 gf load for a dwell time of 30s. Vickers micro-hardness at 600℃ were measured using a high-temperature Vickers hardness indenter (Archimedes HTV-PHS30) under a 3000 gf for a dwell time of 5s. Nano-hardness and elastic modulus were measured using a Hysitron TI-950 Triboindenter (Bruker Corporation, Minneapolis, Minnesota, USA) with a diamond Berkovich tip and cali- brated with standard aluminum and fused quartz.

2.5. Tribological testing

TiMoNb alloy disks with a diameter of 15 mm and alumina ball counterparts with a diameter of 6 mm were used for ball-on-disk wear tests (in accordance with ASTM G99-17). Before wear testing, the surfaces of the sample disks were grinded using SiC grinding papers with grit sizes down to 1200 grit to achieve a surface rough- ness of $R_a < 0.05\mu m$, $R_q < 0.05\mu m$, and $R_z < 0.2\mu m$. The surface profile of the as-grinded TiMoNb alloy is presented in Fig. S1. Ball-on-disk wear tests (THT, Anton-Paar Ball-on-Disk Tribometer, Anton Paar GmbH, Graz, Austria) were performed at RT in air with a relative humidity 50% and at 600℃ under dry sliding condition with a normal load of 5N, a sliding velocity of 0.1 ms^{-1}, and a sliding distance of 1000m. Wear rates of the alloy were determined by a volume loss method, where the surface profiles of the wear tracks were

obtained using a 3D optical microscope (ContourGT-K, Bruker Corporation, Billerica, Massachusetts, USA). A reference surface was determined to quantify the volume of a wear scar, and the volume of materials below the reference surface was taken as the wear volume. Three separate tests were run for each specimen, and the average wear rates and coefficients of friction (CoFs) along with standard deviations were provided.

3. Results

3.1 Phase evolution during ball milling

The XRD patterns of the equiatomic Ti, Mo, and Nb powder mixture before and after ball milling are displayed in Fig 1. In the starting powder mixture, all a-Ti, bcc-Mo, and bcc-Nb diffraction peaks are clearly observed (Fig. 1a). After ball milling for 3h and 6h, the diffraction peaks of Ti, Mo, and Nb gradually disappeared (Fig. 1b) resulting from the ball milling induced mechanical alloying in which the solid solutions are formed. The severe plastic deformation (SPD) induced by ball milling finally instigates the starting powder mixture of α-Ti and bcc-Mo and bcc-Nb into formation of a nanostructured single-phase bcc solid solution after 12h of ball milling (Fig. 1b). Further extending the ball milling times to 18h and 24h only broadens the three bcc diffraction peaks, but without obvious shift of the peak position, indicating smaller grain size and larger strain in the aforementioned nanostructured single-phase bcc solid solution instead of formation of new solid solutions. Note that the additional very weak peak at $2\theta = 44.75°$ originates from the Fe contamination during ball milling.

3.2 Microstructure of the fabricated TiMoNb alloy

The obtained bulk TiMoNb alloy has the relative density exceeding 99%. The XRD pattern shows only a bcc phase in the bulk TiMoNb alloy (Fig. 2a). EBSD inverse pole figure map reveals that the alloy consists of equiaxed bcc grains with an average grain size of 160 nm (Fig. 2b). However, the HAADF-STEM image (Fig. 2c) shows two contrasts. Corresponding bright-field TEM image (Fig. 2d) shows that the dark precipitates are primarily located at the GBs or the triple junctions of the matrix grains. Selected area electron diffraction (SAED) analysis confirms the bcc structure of the alloy (inset in Fig. 2d), consistent with the XRD and EBSD results. EDS elemental maps show that the bright matrix grains are rich in Mo and Nb, whereas the dark precipitates are rich in Ti (Fig. 2e). EDS quantitative analysis shows that the matrix and the Ti-rich precipitates contains 24 ± 3 at.% and 67 ± 16 at.% Ti, respectively. Statistical measurements of 396 grains from STEM/TEM images show that the alloy contains ~93vol.% matrix phase (denoted as B_1 phase) with an average grain size of 188nm and ~7vol.% Ti-rich phase (denoted as B_2 phase) with an average grain size of 79nm. Both grain sizes of B_1 (50—450nm) and B_2 (20 200 nm) phases follow a normal distribution (Fig. 2f and 2g).

HRTEM analysis was performed to investigate the interface orientation relationship between the nanoscale B_2 precipitates and the UFG B_1 matrix. The nanoscale B_2 precipitates are fully coherent with the B_1 matrix with cube-on-cube orientation relationship (Fig. 3a—3c). Both B_1 and B_2 phases are bcc-structured and have very close lattice constants ($\alpha = \sim 3.25$Å), which explains why they cannot be distinguished in XRD, EBSD, and SAED patterns. Fig. 3d displays the HRTEM image of two neighboring B_1 grains, between which a composition and distribution of the three constituent elements in grain interior and at GBs, APT characterization was performed, which is capable of both 3D imaging and quantitative chemical analysis. 3D reconstruction of 50 at.% Ti isoconcentration surface (Fig. 3e and 3f) reveals the composition difference between B_1 matrix and B_2 precipi- tates. B_1 matrix grain

interior contains 22 at.% Ti, 50 at.% Mo and 27 at.% Nb, while the B_2 precipitates contain 65 at.% Ti, 30 at.% Mo and 5 at.% Nb. This result is consistent with the above STEM-EDS analysis, in which the Ti concentration in B_2 precipitates is approximately three times that of B_1 matrix. The composition difference between the two separated bcc phases can be attributed to the enthalpies of mixing among the three constituent e lements ($\Delta H_{TiNb}^{mix} = 2kJ/mol$, $\Delta H_{TiMo}^{mix} = -4kJ/mol$, and $\Delta H_{MoNb}^{mix} = -6kJ/mol$)[42]. The most negative value of ΔH_{MoNb}^{mix} Energeically favors the formation of (Mo , Nb)-rich matrix phase and the more negative value of ΔH_{TiMo}^{mix} than ΔH_{TiNb}^{mix} explains the Ti-rich phase contains more Mo than Nb. Atom map of Ti (Fig. 3g) across two abutting B_1 grains clearly demonstrates Ti atoms segregation at the GBs, forming intergranular films with a thickness of 1~5nm. One-dimensional concentration profiles (Fig. 3h) indicate that the Ti concentration at GB reaches ~27 at.%, approximately 5 at.% higher than that of the matrix grain interior. The segregation of Ti atoms to the GBs would reduce the lattice distortion (note that Ti has the largest atomic radius) and consequently reduce the total free energy of the system. According to these analyses, we schematically illustrate the microstructure of bulk TiMoNb alloy in Fig. 3i, which consists of a primary UFG B_1 matrix with Ti atoms segregation at the GBs and a high density of coherent, nanoscale B_2 precipitates.

3.3 *Hardness and wear performance*

Since wear resistance empirically correlates with material's hardness, prior to wear test, we first measured the hardness of the alloy at the target wear test temperatures. The microhardness of the fabricated alloy reaches up to 651.5 ± 10.4HV at RT and slightly decreases to 584.3 ± 13.4HV at 600°C.

At RT, the wear reached a steady state after an initial running-in period with a sliding distance of ~25 m (Fig. 4a). The steady state CoF was measured to be 0.86 ± 0.01. Generally, in studies that assess wear of materials, much harder counterfaces (compared with the test material) are used so that wear is predominantly due to the material of interest [3]. Notably, for the evaluation of UFG TiMoNb alloy, the counterface alumina balls were severely worn (insets in Fig. 4a) despite having a hardness (1500HV) over twice higher than that of the alloy. The calculated wear rates of the samples and alumina ball counterparts were 5.60(± 0.28) × $10^{-4}$$mm^3$/(Nm) and 1.61 (± 0.50) × $10^{-4}$$mm^3$/(Nm), respectively. The results suggest that UFG TiMoNb alloy exhibits comparable wear resistance to alumina at RT, despite that the absolute value of the wear rates does not truly reflect the exceptional wear resistance of the present alloy as the counterface alumina balls were severely worn. Top-view SEM images (Fig. 4b) show the surface appearance of the wear track, which is ~4μm wide and characterized by fatigue wear traces and severe adhesion. The wear track has the surface roughness of R_a = 1.27 ± 0.23μm, R_q = 1.58 ± 0.29μm, and R_z = 10.92 ± 1.76μm. EDS analysis of the wear track (Fig. 4c and Fig. S2) indicates that in addition to Ti, Mo, and Nb, from the alloy, the worn surface contains Al and O elements from the alumina ball counterpart. The wear debris consists of mainly fine particles in size ranging from 0.2 to 2.0μm and a minor amount of large fragments with size ranging from 10 to 40μm (Fig. 4d). EDS chemical analysis (Fig. 4e) and XRD (Fig. 4f) confirms that the wear debris comprises both Al_2O_3 and bcc TiMoNb alloy from the tribopair. The XPS survey scan spectrum of the worn surface (Fig. S3a) shows the main peaks of Nb 3p, 3d, Mo 3p, 3d and Ti 2p along with the Al 2s and 2p from the transferred Al_2O_3 counter body. The high-resolution XPS spectra (Fig. 5) further reveal that besides the metallic Ti 2p at 454.0 eV, Mo 3d at 227.4 eV and Nb 3d at 202.3 eV, peaks of oxides including TiO_2 (458.9 eV), MoO_2 (230.7 eV), MoO_3 (232.5 eV), NbO (203.3 eV) and Nb_2O_5 (207.4

eV) were also observed, indicating that the worn surface was slightly oxidized. In contrast to Ti 2p (Fig. 5a) and Nb 3d (Fig. 5c) spectra with very low relative intensity of metallic state, the Mo 3d (Fig. 5b) shows strong metallic Mo peaks, suggesting higher oxidation resistance of Mo than those of Ti and Nb.

Upon wear exposure at 600℃, the steady state CoF of TiMoNb alloy decreased to be 0.72 ± 0.02 (Fig. 6a). Under this wear condition, the alumina ball counterparts show no detectable wear. In comparison with wear tracks observed on TiMoNb disk at RT, the wear tracks at 600℃ are much smaller, ~0.4mm wide, and featured with traces of oxidative and abrasive wear characteristics (Fig. 6b). The wear track at 600℃ has the surface roughness of R_a = 0.39 ± 0.09μm, R_q = 0.51 ± 0.10μm, and R_z = 7.63 ± 1.53μm. For the calculation of volume loss of the TiMoNb alloy, the wear track profile was integrated to obtain the average cross-sectional area (Fig. 6c and 6d), then the wear volume loss was calculated by multi- plying average track cross-section area and the track length. The measured wear rate was determined to be 3.15 (± 0.50) × $10^{-6}$$mm^3$/(Nm). Such a wear rate is extremely low for metallic alloys subjected to dry sliding wear at an elevated temperature of 600℃. EDS analysis (Fig. 6f for Location 1 in Fig. 6b) reveals that the surface was oxidized and Al_2O_3 was not transferred to the wear track. The wear debris comprises fine equiaxed particles in size ranging from 0.25 to 10μm (Fig. 6e). EDS analysis (Fig. 6f for Location 2 in Fig. 6b) shows that besides the ball and disk materials, Ti-, Mo-, and Nb-based oxides were detected in the wear debris. Note that the small amount of wear debris is not enough for phase identification by XRD. EDS mapping analysis of the wear track in Fig. S4 further confirms that no bulk oxides are aggregated on the surface of the sample. XPS survey scan spectrum of the wear track at 600℃ shows almost no alumina, distinct from that of the wear track at RT. Moreover, the high-resolution XPS spectra (Fig. 7) show the strong peaks of oxides, but no metallic

state peaks were present, suggesting that the surface of wear track at 600℃ is covered with an oxide layer composed of TiO_2, MoO_3 and Nb_2O_5 (Fig. 7).

4. Discussion

4.1 Wear at RT

We firstly rationalize the exceptional wear resistance of the UFG TiMoNb alloy at RT. The maximum Hertzian contact pressure σ_{max} was estimated to be 1.26 GPa, much below the measured hardness at RT (651.5 ± 10.4HV) as well as at 600℃ (584.3 ± 13.4HV). At RT, the TiMoNb alloy shows wear resistance comparable to alumina but with a high CoF. The wear modes are dominantly stress-driven fatigue wear and severe adhesive wear. To seek the origin of the exceptional wear resistance, the ND-SD cross-sectional microstructure below the sliding surface was examined, as presented in Fig. 8. The shear strain, induced by sliding, breaks down the original equiaxed grain structure to form elongated grains. The plastic deformation region has a very shallow depth, extending only to a depth of ~1.2μm away from the sliding surface (Fig. 8a, b), suggesting high flow stress of the alloy. Despite the presence of oxides in XPS spectra (Fig. 5), no glaze layer or mechanical mixing layer was observed suggesting the extremely small thickness of the passive oxide layer. To reveal the deformation mechanism of the B_1 matrix grains, HRTEM analysis on a representative topmost layer with thickness of ~50nm were performed (Fig. 8c). The severely deformed matrix grains contain a considerable number of stacking faults (marked as SF in Fig. 8d) and a high density of dislocations (Fig. 8e), which would produce additional strain hardening and strengthening[43]. The elongation of the B_2 phase along the SD was also observed (Fig. 9), which occurs only in the topmost 800nm. On the

basis of the above obser- vations, we attribute the exceptional wear resistance of the present alloy at RT to four factors: (1) GB strengthening (Hall-Petch strength- ening) from the UFG matrix; (2) segregation of Ti atoms at GBs mitigating the stress-driven microstructure evolution during wear and thus suppressing delamination wear; (3) additional precipitation strengthening due to the presence of a high density of coherent nanoscale Ti-rich B_2 precipitates; and (4) the intrinsic solid solution strengthening of the alloy matrix.

To investigate the sliding-induced damage accumulation in TiM-oNb alloy and wear mechanism, we also examined the surface morphology (Fig. 10) after 1, 5, 10, and 20 sliding cycles at the early stage of wear. After one single sliding pass, a 0.34μm-deep wear scar is gen- erated and the worn surface is featured with delamination, pileups of submicron heights, and plow furrows (Fig. 10a). After sliding for 5 cycles, the worn surface is mainly featured with fish-scale-like patterns perpendicular to SD with a small number of plow furrows (Fig. 10b). After sliding cycles of 10 (Fig. 10c) and 20 (Fig. 10d), the surface continues to be roughened and the transfer material of alumina was also detected. Since the fatigue wear process proceeds by subsurface deformation, crack nucleation, and crack propagation, the ND-SD cross-sectional microstructure below the sliding surface after one single pass was examined to seek for the crack initiation sites of the alloy during wear (Fig. 11). The nanoscale cracks were frequently located at the B_1 matrix/B_2 precipitate or B_2/B_2 interfaces (as indicated by the yellow arrows in Fig. 11d). The number of cracks increases upon approaching the sliding surface. These observations suggest that the cracks initiate in the subsurface layer, predominantly at the B_1 matrix/ B_2 preciptate interfaces. The nanoscale cracks propagate during repeated sliding, which results in t he formation of the debris. Fig.4b also suggests severe adhesive wear. To explain the presence of the alumina counter body (Fig. S5). SEM images (Fig.S5a-b) with EDS analysis (Fig. S5c-f) clearly

shows the TiMoNb alloy transfer to the surface of alumina, despite that the transferred alloy covers only some local areas of the alumina surface. The alloy transfer to the sounter body would lead to the local alloy against alloy contact and the presence of severe adhesive wear.

We then analyzed the high CoF during sliding against alumina at RT. Dry sliding wear of titanium alloys on ceramic typically shows high CoF, e.g. Ti6Al4V sliding against alumina ball shows CoF of 0.4—0.75 depending on sliding velocity and applied load[12,44], ultra-fine grained Ti sliding against diamond shows the CoF of ~0.6[45]. As is known, the friction properties largely depend on the roughness of the contact surface, including the distribution, height and deformation of the asperities[46 49] and materials transfer during wear. To explain the relatively higher CoF of the present alloy, we also examined surface roughness and material transfer during wear. As mentioned above, the as-grinded TiMoNb alloy before sliding wear has $R_a < 0.05\mu m$, $R_q < 0.08\mu m$ and $R_z < 0.2\mu m$ (Fig. S1). After sliding for 1 cycle, the surface roughness has increased to be R_a=0.32μm, R_q=0.52μm, and R_z=0.88μm (Fig. S6). After 5 cycles, the surface roughness shows a significant increase with R_a=1.35μm, R_q=1.98μm and R_z= 7.51μm (Fig. S7). After sliding cycles of 10 and 20, the surface continues to be roughened (Fig. S8-S9). Even after sliding over 1000m, the surface roughness R_a and R_q are still over 1 mm and R_z reaches up to several microns. The large surface roughness would lead to high friction. In addition, the TiM-oNb alloy transfer to the counter body (alumina) (Fig. S5) would also reduce direct contact of alumina and the alloy. The local alloy against alloy contact would also increase the CoF. Therefore, the high friction could be attributed to the severe surface roughening and the TiMoNb alloy material transfer to the counter body during wear.

4.2 Wear at 600℃

Upon wear exposure at 600℃, TiMoNb alloy displays an extremely lower wear rate of the order of 10^{-6} $mm^3/(N\ m)$ and reduced friction when compared with the corresponding alloy tested at RT. The fluctuation of the CoF, frequently observed during sliding wear at elevated temperatures[1], is attributed to the dynamic process of the formation of the glaze layer which involves transient oxidation and removal of the transient oxides on each sliding cycle[50,51]. Compared with the surface roughness of the wear track at RT, the surface roughness of the wear track at 600℃ decreased to be R_a = 0.39 ± 0.09μm, R_q = 0.51 ± 0.10μm, and but R_z still has a high value of 7.63 ± 1.53μm, which suggests that the thickness of the glaze layer is not uniform. This can be confirmed by the crinkled surface observed in Fig. 6b. These results explain the relatively high CoF at 600℃ even with the presence of the glaze layer. To make sure that the tribosystem has reached steady-state wear, we further extended the sliding distance to 1500m (with the total sliding time of up to 4h and 10min) and compared the CoF, wear rate and morphology (Fig. S10-S11) with those of after 1000m. It is found that the measured average CoF (0.72) and the wear rate (3.55 10^{-6} $mm^3/(N\ m)$) (Fig. S10) are very close to those of after sliding for 1000 m. In addition, their wear tracks also show similar morphology (Fig. S11). All these information confirms that tribosystem has reached steady-state wear after sliding for 1000m.

The study of wear track and debris by SEM and EDS (Fig. 6) also suggest a distinct wear mechanism from that observed at RT. ND-SD cross-sectional microstructural analysis (Fig. 12) shows that thermomechanical actions lead to the formation of a gradient microstructure along the depth away from the sliding surface. In contrast to the small deformation depth generated at RT, the sliding wear-induced plastic deformation extends to a larger depth of ~6μm In the topmost region, extending from

sliding surface to a depth of ~200nm, a dense glaze layer is formed, as indicated in the HAADF-STEM image in Fig. 12a. This glaze layer comprises randomly orientated equiaxed nanograins with an average grain size of only 9 nm (Fig. 12c—f). EDS elemental maps (Fig. 12b) and SAED pattern (Fig. 12f) reveal that this layer consists of primarily Ti, Mo, and Nb oxides (e.g. Nb_2O_5 and TiO_2), consistent with the compositional analysis by XPS (Fig. 7), and a small amount of bcc alloy. It should be noted that the chemical composition analyzed by XPS is only limited in the topmost several nanometers of the glaze layer. It is also found that there is a slight Mo depletion in the glaze layer, which might be attributed to the relatively higher oxidation resistance of Mo than those of Ti and Nb, as confirmed by the XPS spectra in Fig. 5. The faster formation of Ti- and Nb-oxides could deplete more Ti and Nb atoms in the alloy near the glaze layer and thus increase the concentration gradients of these two solute atoms which would facilitate their atomic diffusion to the sliding surface. The slight depletion in Mo may cause mechanical softening in the topmost layer and affect the friction and wear properties of the alloy, as demonstrated by the reduced CoF and more severe plastic deformation near the sliding surface at 600℃ (Fig. 12). Below the equiaxed nanocrystalline glaze layer, extending to a depth of ~2.6μm is a severely deformed region, where the matrix B_1 phase is elongated into layers. More interestingly, the Ti-rich B_2 precipitates get much larger than in the undeformed bulk, and the intergranular films between the two abutting deformed B_1 matrix grains get thicker in this region (Fig. 12a). A selected representative region containing B_2 precipitate and intergranular films was characterized in detail (Fig. 12g—l). It should be noted that the growth of the Ti-rich B_2 precipitates and the increase in the thickness of intergranular films between B_1 grain boundaries only occur in the high-temperature wear experiments, not those at RT and also, they do not occur below the SPD surface region. These observations might be attributed to strain-enhanced diffusion at high-temperature[52,53], where plastic deformation could create excess

vacancies, and these vacancies could enhance solute diffusion[54—56] and thus promote the segregation of Ti atoms at the GBs and growth of the B_2 precipitates [57,58]. This may increase the plasticity in the near-surface region at high temperatures. The extremely low diffusivities of Ti in Mo (1.882×10^{-17} mm^2/s)[59] and Nb (in the order of 10^{-16} mm^2/s)[60] explain why no precipitate growth far below the sliding surface. At the greater depth, extending to 6 mm away from the surface, is a moderately plastic deformation region. The individual grains become more and more equiaxed with increasing depth and gradually recover to the original (undeformed) state.

To investigate potential occurrence of grain coarsening during the wear process (600℃ for ~3h), the microstructure of the undeformed matrix far away from the sliding surface (Fig. 13) was examined. The average sizes of B_1 grains and B_2 precipitates were measured to be 208 and 95nm, respectively. In comparison with the as-fabricated alloy, such a slight increase in grain/precipitate size indicates that the present UFG TiMoNb HEA has excellent thermal stability, as also confirmed by the slight reduction in hardness from RT to 600 °C.

Based on these findings, we believe that the following three factors are mainly responsible for the exceptional wear resistance of UFG TiMoNb alloy at elevated temperature. First, the formation of a dense glaze layer comprising nanocrystalline equiaxed metallic oxides could reduce the contact shear strength of the sliding interfaces and thus results in a lower CoF. Furthermore, the glaze layer could protect the disk substrate from severe wear and thus contribute to the ultralow wear rate[9]. Second, the enhanced Ti atoms segregation at high temperature reduces the GB energy and thermodynamically stabilizes the UFG structure. Last but not least, the coherent B_2 nanoprecipitates located at the GBs and triple junctions could pin GBs within TiMoNb alloy, which further increases the energy barrier for GB sliding and rotation, thus inhibiting thermal softening and grain coarsening[61].

The obtained results offer significant insights into the design of strong, wear-resistant, and thermo-mechanically stable alloys for service in harsh environments. This study also extends the use of complexion engineering in CCAs with multi-principal elements and suggest important and interesting direction for future research in HEAs/CCAs.

5. Conclusions

A UFG equiatomic TiMoNb alloy was fabricated using high-energy ball milling and SPS. The alloy consists of two bcc phases: ~93vol.% of B_1 matrix with an average grain size of 188nm and ~7vol.% Ti-rich B_2 precipitate phase with an average grain size of 79nm. Interestingly, Ti atoms segregation was found at the GBs of B_1 matrix, forming intergranular films with a thickness of 1~5nm and the Ti concentration approximately 5 at.% higher than that of the matrix grain interior. The nanoscale B_2 precipitates were fully coherent with the B_1 matrix with cube-on-cube orientation relationship.

The particular microstructure enables high thermal stability and exceptional wear resistance both at RT and 600℃. At RT, the wear resistance was even comparable to alumina with two-folds higher hardness. The plastic deformation region had a very shallow depth of only ~1.2μm away from the sliding surface with a considerable number of stacking faults and a high density of dislocations present in the severely deformed matrix grains. At 600℃, the alloy still showed an extremely low wear rate of the order of 10^{-6} $mm^3/(Nm)$, but the sliding wear-induced plastic deformation extended to a larger depth of ~6μm and the formation of a gradient microstructure: (I) a dense equiaxed nanocrystalline glaze layer in the topmost ~200μm, (II) a severely deformed region between 200nm and 2.6μm, with the matrix

B_1 phase elongated into layers, and (III) a moderately deformed region. More interestingly, much larger Ti-rich B_2 precipi- tates and much thicker intergranular films between the two abutting deformed B_1 matrix grains than in the un-deformed bulk were found in Region II, which may be attributed to the strain-induced diffusion which thus promotes the segregation of Ti atoms at the GBs and growth of the B_2 precipitates at high temperature.

Declaration of Competing Interest

The authors declare no conflict of interest.

Acknowledgments

The authors sincerely thank Prof. Robert S. Averback in University of Illinois at Urbana-Champaign for stimulating discussions and constructive comments. This work was financially supported by the Fundamental Research Program of Shenzhen (Grant No. JCYJ20170412153039309), and Guangdong Innovative & Entrepreneurial Research Team Program (No. 2016ZT06C279). APT research was conducted at the Inter-University 3D APT Unit of City University of Hong Kong (CityU), which is supported by the CityU grant 9360161. This work was also supported by the Pico Center at SUS-Tech that receives support from Presidential fund and Development and Reform Commission of Shenzhen Municipality.

References

1.P.J. Blau, Elevated-temperature tribology of metallic materials, Tribol. Int. 43 (7) (2010) 1203–1208.

2. X. Chen, Z. Han, X. Li, K. Lu, Lowering coefficient of friction in Cu alloys with stable gradient nanostructures, Sci. Adv. 2 (12) (2016) e1601942.

3. J.F. Curry, T.F. Babuska, T.A. Furnish, P. Lu, D.P. Adams, A.B. Kustas, B.L. Nation, M.T. Dugger, M. Chandross, B.G. Clark, B.L. Boyce, C.A. Schuh, N. Argibay, Achiev- ing ultralow wear with stable nanocrystalline metals, Adv. Mater. 30 (32) (2018) e1802026.

4. E. Svanidze, T. Besara, M.F. Ozaydin, C.S. Tiwary, J.K. Wang, S. Radhakrishnan, S. Mani, Y. Xin, K. Han, H. Liang, T. Siegrist, P.M. Ajayan, E. Morosan, High hardness in the bio compatible intermetallic compound b-Ti3Au, Sci. Adv. 2 (7) (2016) e1600319.

5. D.A.Rigey, Transfer, mixing associated chemical and mechancal processes during the sliding of ductile materials, Wear 245(1-2)(2000)1-9.

6. T.J. Rupert, C.A. Schuh, Sliding wear of nanocrystalline Ni W: structural evolution and the apparent breakdown of Archard scaling, Acta Mater. 58 (12) (2010) 4137–4148.

7. F. Ren, S.N. Arshad, P. Bellon, R.S. Averback, M. Pouryazdan, H.C. Hahn, Sliding wear-induced chemical nanolayering in Cu Ag, and its implications for high wear resistance, Acta Mater. 72 (2014) 148–158.

8. C. Greiner, J. Gagel, P. Gumbsch, Solids under extreme shear: friction-mediated subsurface structural transformations, Adv. Mater. 31 (26) (2019) 1806705.

9. F.H. Stott, High-temperature sliding wear of metals, Tribol. Int 35 (8) (2002) 489–495.

10. K.G. Budinski, Tribological properties of Titanium-alloys, Wear 151 (2) (1991) 203–217.

11.D. Ku€mmel, M. Hamann-Schroer, H. Hetzner, J. Schneider, Tribological behavior of nanosecond-laser surface textured Ti6Al4V, Wear 422 (2019) 261–268.

12. H. Dong, T. Bell, Tribological behaviour of alumina sliding against Ti6Al4V in unlu- bricated contact, Wear 225-229 (1999) 874–884.

13. M. Long, H.J. Rack, Titanium alloys in total joint replacement—a materials science perspective, Biomaterials 19 (18) (1998) 1621–1639.

14. M. Geetha, A.K. Singh, R. Asokamani, A.K. Gogia, Ti based biomaterials, the ulti- mate choice for orthopaedic implants A review, Prog. Mater. Sci. 54 (3) (2009) 397–425.

15. R. Dong, W. Zhu, C. Zhao, Y. Zhang, F. Ren, Microstructure, mechanical properties, and sliding wear behavior of spark plasma sintered Ti-Cu alloys, Metall. Mater. Trans A 49 (12) (2018) 6147–6160.

16. R. Valiev, Nanostructuring of metals by severe plastic deformation for advanced properties, Nat. Mater. 3 (8) (2004) 511–516.

17. P. La, J. Ma, Y.T. Zhu, J. Yang, W. Liu, Q. Xue, R.Z. Valiev, Dry-sliding tribological properties of ultrafine-grained Ti prepared by severe plastic deformation, Acta Mater. 53 (19) (2005) 5167–5173.

18. N. Saka, J.J. Pamies-Teixeira, N.P. Suh, Wear of two-phase metals, Wear 44 (1) (1977) 77–86.

19. K. Lu, Stabilizing nanostructures in metals using grain and twin boundary archi- tectures, Nat. Rev. Mater. 1 (5) (2016) 1–13.

20. P.R. Cantwell, M. Tang, S.J. Dillon, J. Luo, G.S. Rohrer, M.P. Harmer, Grain boundary complexions, Acta Mater. 62 (2014) 1–48.

21. T. Chookajorn, H.A. Murdoch, C.A. Schuh, Design of stable nanocrystalline alloys, Science 337 (6097) (2012) 951–954.

22. A.R. Kalidindi, C.A. Schuh, Stability criteria for nanocrystalline alloys, Acta Mater. 132 (2017) 128–137.

23. H.A. Murdoch, C.A. Schuh, Stability of binary nanocrystalline alloys against grain growth and phase separation, Acta Mater. 61 (6) (2013) 2121–2132.

24. A. Khalajhedayati, Z. Pan, T.J. Rupert, Manipulating the interfacial structure of nanomaterials to achieve a unique combination of strength and ductility, Nat. Commun. 7 (2016) 10802.

25. T.J. Rupert, The role of complexions in metallic nano-grain stability and deforma- tion, Curr. Opin. Solid State Mater. Sci. 20 (5) (2016) 257–267.

26. C.M. Grigorian, T.J. Rupert, Thick amorphous complexion formation and extreme thermal stability in ternary nanocrystalline Cu-Zr-Hf alloys, Acta Mater. 179 (2019) 172–182.

27. J.D. Schuler, T.J. Rupert, Materials selection rules for amorphous complexion for- mation in binary metallic alloys, Acta Mater. 140 (2017) 196–205.

28. B. Gludovatz, A. Hohenwarter, D. Catoor, E.H. Chang, E.P. George, R.O. Ritchie, A fracture-resistant high-entropy alloy for cryogenic applications, Science 345 (6201) (2014) 1153–

1158.

29. Z. Li, K.G. Pradeep, Y. Deng, D. Raabe, C.C. Tasan, Metastable high-entropy dual- phase alloys overcome the strength-ductility trade-off, Nature 534 (2016) 227–230.

30. B. Gludovatz, A. Hohenwarter, K.V.S. Thurston, H. Bei, Z. Wu, E.P. George, R.O. Ritchie, Exceptional damage-tolerance of a medium-entropy alloy Crconi at cryogenic temperatures, Nat. Commun. 7 (2016) 10602.

31. Z. Fu, L. Jiang, J.L. Wardini, B.E. MacDonald, H. Wen, W. Xiong, D. Zhang, Y. Zhou, T.J. Rupert, W. Chen, E.J. Lavernia, A high-entropy alloy with hierarchical nanopre- cipitates and ultrahigh strength, Sci. Adv 4 (10) (2018) eaat8712.

32. S.S. Sohn, A. Kwiatkowski da Silva, Y. Ikeda, F. Ko€rmann, W. Lu, W.S. Choi, B. Gault, D. Ponge, J. Neugebauer, D. Raabe, Ultrastrong medium-entropy single-phase alloys designed via severe lattice distortion, Adv. Mater. 31 (8) (2019) 1807142.

33. Z. Lei, X. Liu, Y. Wu, H. Wang, S. Jiang, S. Wang, X. Hui, Y. Wu, B. Gault, P. Kontis, D. Raabe, L. Gu, Q. Zhang, H. Chen, H. Wang, J. Liu, K. An, Q. Zeng, T.-.G. Nieh, Z. Lu, Enhanced strength and ductility in a high-entropy alloy via ordered oxygen com- plexes, Nature 563 (7732) (2018) 546–550.

34. K. Lu, L. Lu, S. Suresh, Strengthening materials by engineering coherent internal boundaries at the nanoscale, Science 324 (5925) (2009) 349–352.

35. B. Predel, Mo-Ti (Molybdenum-Titanium), in: O. Madelung (Ed.), Springer Berlin Heidelberg, Berlin, Heidelberg, 1997, pp. 1–3. Li-Mg-Nd-Zr.

36. B. Predel, Nb-Ti (Niobium-Titanium), in: O. Madelung (Ed.), Springer Berlin Hei- delberg, Berlin, Heidelberg, 1997, pp. 1–3. Li-Mg Nd-Zr.

37. P. Franke, D. Neuschu€tz, Mo-Nb, in: P. Franke, D. Neuschu€tz (Eds.), Binary Sys- tems. Part 4: Binary Systems from Mn-Mo to Y-Zr: Phase Diagrams, Phase Transi- tion Data, Integral and Partial Quantities of Alloys, Springer Berlin Heidelberg, Berlin, Heidelberg, 2006, pp. 1–4.

38. Q. Chen, G.A. Thouas, Metallic implant biomaterials, Mat. Sci. Eng. R 87 (2015) 1–57.

39. L.H. de Almeida, I.N. Bastos, I.D. Santos, A.J.B. Dutra, C.A. Nunes, S.B. Gabriel, Corro- sion resistance of aged Ti Mo Nb alloys for biomedical applications, J. Alloys Compd. 615 (2014) S666–S669.

40. J. Dai, J. Zhu, C. Chen, F. Weng, High temperature oxidation behavior and research status of modifications on improving high temperature oxidation resistance of titanium alloys and titanium aluminides: a review, J. Alloys Compd. 685 (2016) 784–798.

41. G.G. Vladimir Cheverikin, Alina Makudera, Jean Claude Tedenac, M. Materials Sci- ence International Team, Isothermal section At 600°C [1958Kor, 1961Eng].: Datasheet from MSI Eureka in SpringerMaterials

(https://materials.springer.com/msi/phase-

diagram/docs/sm_msi_r_10_021856_01_full_LnkDia2), in: G. Effen- berg (Ed.) MSI, Materials Science International, Stuttgart.

42. A. Takeuchi, A. Inoue, Classification of bulk metallic glasses by atomic size differ- ence, heat of mixing and period of constituent elements and its application to char- acterization of the main

alloying element, Mater. Trans. 46 (12) (2005) 2817–2829.

43. Y.L. Zhao, T. Yang, Y. Tong, J. Wang, J.H. Luan, Z.B. Jiao, D. Chen, Y. Yang, A. Hu, C.T. Liu, J.J. Kai, Heterogeneous precipitation behavior and stacking-fault-medi- ated deformation in a Cocrni-based medium-entropy alloy, Acta Mater 138 (2017) 72–82.

44. H. Dong, A. Bloyce, P.H. Morton, T. Bell, Surface engineering to improve tribologi- cal performance of Ti 6Al 4V, Surf. Eng. 13 (5) (1997) 402–406.

45. C.T. Wang, N. Gao, M.G. Gee, R.J.K. Wood, T.G. Langdon, Effect of grain size on the micro-tribological behavior of pure titanium processed by high-pressure torsion, Wear 280-281 (2012) 28–35.

46. X. Chen, Z. Han, K. Lu, Friction and wear reduction in copper with a gradient nano- grained surface layer, ACS Appl. Mater. Inter. 10 (16) (2018) 13829–13838.

47. H.A. Padilla, B.L. Boyce, C.C. Battaile, S.V. Prasad, Frictional performance and near- surface evolution of nanocrystalline Ni Fe as governed by contact stress and slid- ing velocity, Wear 297 (1) (2013) 860–871.

48. P. Stoyanov, P. Stemmer, T.T. Ja€rvi, R. Merz, P.A. Romero, M. Scherge, M. Kopnarski, M. Moseler, A. Fischer, M. Dienwiebel, Friction and wear mechanisms of Tungsten Carbon systems: a comparison of dry and lubricated condi- tions, ACS Appl. Mater. Int. 5 (13) (2013) 6123–6135.

49.M. Sahin, C.S. C¸ etinarslan, H.E. Akata, Effect of surface roughness on friction coeffi- cients during upsetting processes for different materials, Mater. Des. 28 (2) (2007) 633–640.

50. C. Rynio, H. Hattendorf, J. Klo€wer, G. Eggeler, The evolution of tribolayers during high

temperature sliding wear, Wear 315 (1) (2014) 1–10.

51. F.H. Stott, The role of oxidation in the wear of alloys, Tribol. Int. 31 (1) (1998) 61–71.

52. H. Mecking, Y. Estrin, The effect of vacancy generation on plastic deformation, Scripta Metal. Mater. 14 (7) (1980) 815–819.

53. M. Militzer, W.P. Sun, J.J. Jonas, Modelling the effect of deformation-induced vacancies on segregation and precipitation, Acta Metal. Mater. 42 (1) (1994) 133–141.

54. R.W. Balluffi, A.L. Ruoff, On strain enhanced diffusion in metals. I. point defect models, J. Appl. Phys. 34 (6) (1963) 1634–1647.

55. S.H. Song, X.M. Chen, L.Q. Weng, Solute diffusion during high-temperature plastic deformation in alloys, Mater. Sci. Eng. A 528 (24) (2011) 7196–7199.

56. T. Watanabe, S. Karashima, On the strain-enhanced diffusion of a-iron, Phys. Stat. Sol. 42 (2) (1970) 749–756.

57. P. Bellon, R.S. Averback, Nonequilibrium roughening of interfaces in crystals under shear: application to ball milling, Phys. Rev. Lett. 74 (10) (1995) 1819–1822.

58. T. Klassen, U. Herr, R.S. Averback, Ball milling of systems with positive heat of mixing: effect of temperature in Ag-Cu, Acta Mater. 45 (7) (1997) 2921–2930.

59. L. Feng, J.S. Li, L. Huang, H. Chang, Y.W. Cui, L. Zhou, Interdiffusion behavior of Ti- Mo binary system in b phase, Chin. J. Nonferrous Met. 19 (10) (2009) 1766–1771.

60. F. Roux, A. Vignes, Diffusion dans les syste`mes Ti-Nb, Zr-Nb, V-Nb, Mo-Nb, W-Nb, Rev. Phys. Appl. 5 (3) (1970) 393–405.

61. K.A. Darling, M. Rajagopalan, M. Komarasamy, M.A. Bhatia, B.C. Hornbuckle, R.S. Mishra, K.N. Solanki, Extreme creep resistance in a microstructurally stable nanocrystalline alloy, Nature 537 (7620) (2016) 378–381.

Figure captions

Fig. 1. XRD patterns of the equiatomic Ti, Mo and Nb powder mixture. (a) The starting powder mixture; (b) the powder mixture after ball milling for different times.

Fig. 2. Phase and microstructure of the bulk TiMoNb alloy. (a) XRD pattern; (b) EBSD inverse pole figure map; (c) HAADF-STEM image; (d) bright-field TEM image of (c) and corresponding SAED patterns (inset); (e) EDS elemental maps; (f) grain size distribution of the B_1 matrix and (g) grain size distribution of the B_2 precipitates

Fig. 3. (a) HRTEM image of the two neighboring B_1 and B_2 grains; (b) and (c) are IFFT and corresponding FFT (insets) images of the B_1 and B_2 grains in (a), respectively; (d) HRTEM image of the two neighboring B_1 grains; (e) three-dimensional reconstruction of 50 at.% Ti isoconcentration surface with highlighted B_2 precipitates; (f) proximity histogram showing the composition change across B_1 matrix and B_2 precipitates. Error bars, s.d.; (g) atom map of Ti demonstrating segregation of Ti atoms at the GBs between two abutting B_1 grains; (h) one-dimensional concentration profiles of Ti, Mo and Nb in the selected region in (g) (marked by the gray cylinder); and (i) a schematic diagram shows the microstructure of the TiMoNb alloy.

Fig. 4. Wear characteristics of the bulk TiMoNb alloy upon dry sliding against alumina at RT. (a) Coefficients of friction as a function of sliding distance and optical image of the alumina balls before and after wear tests (insets); (b) SEM images of the wear track; (c) EDS spectra of the typical area in (b); (d) SEM image of the wear debris; (e) typical EDS spectra of the locations marked in (d); and (f) XRD pattern of the wear debris.

Fig. 5. High resolution XPS spectra of Ti 2p, Mo 3d, Nb 3d and Al 2p obtained from the wear track at

RT for 1000m. (a) Ti 2p; (b) Mo 3d; (c) Nb 3d; and (d) Al 2p

Fig. 6. Wear characteristics of the bulk TiMoNb alloy upon dry sliding against alumina at 600℃. (a) Coefficients of friction as a function of sliding distance; (b) SEM images of the wear track; (c) 3D surface profile of wear track; (d) 2D cross-sectional profile along the dotted line (y direction, TD) in (c); (e) SEM image of the wear debris; (f) typical EDS spectra in (b) and (f).

Fig. 7. High resolution XPS spectra of Ti 2p, Mo 3d and Nb 3d obtained from the wear track at 600℃ for 1000m. (a) Ti 2p; (b) Mo 3d; and (c) Nb 3d.

Fig. 8. ND-SD cross-sectional characterization of the TiMoNb alloy after dry sliding against alumina at RT. (a) HAADF-STEM image; (b) bright-field TEM image of the selected area A in (a) with corresponding SAED patterns (insets in (b)); (c) HRTEM image of the topmost layer; (d) and (e) are corresponding inverse fast Fourier transform (IFFT) images of the selected area in (c).

Fig. 9. EDS analysis of the severe plastic deformation region below the sliding surface after wear at RT. (a) ND-SD cross-sectional HAADF-STEM image and (b-d) corresponding EDS elemental maps

Fig. 10. SEM images of the wear track after sliding for different cycles at RT. (a) 1 cycle; (b) 5 cycles; (c) 10 cycles; and (d) 20 cycles. Inset in (d) is an EDS spectrum showing the alu- mina transfer

Fig. 11. (a) SEM image of the wear track after sliding for 1 cycle at RT; (b) SEM image of the selected representative location with the protective platinum (Pt) cap layer for subsur- face analysis; (c) and (d) are low and high magnification SEM images of the selected ND-SD cross-sectional microstructure, respectively. The initiation sites of the cracks were indicated by the yellow arrow.

Fig. 12. ND-SD cross-sectional characterization of the TiMoNb alloy after dry sliding against alumina

at 600℃. (a) HAADF-STEM image; (b) enlarged HAADF-STEM image and corre- sponding EDS elemental maps; (c—f) are bright-field TEM image, HRTEM image, particle size distribution, and SAED pattern of the glaze layer, respectively; (g—i) are HAADF-STEM image, bright-field TEM image and corresponding SAED pattern of the layered B_1 and B_2 phases, respectively; (j—l) are EDS elemental maps of the representative deformed B_1 and B_2 phases, respectively.

Fig. 13. Microstructure of the un-deformed region far away from the sliding surface after wear at 600℃. (a) HAADF-STEM image; (b) EDS elemental maps (scale bar is 200nm); (c) grain size distribution of the B_1 matrix and (d) grain size distribution of the B_2 precipitates.

Fig 1

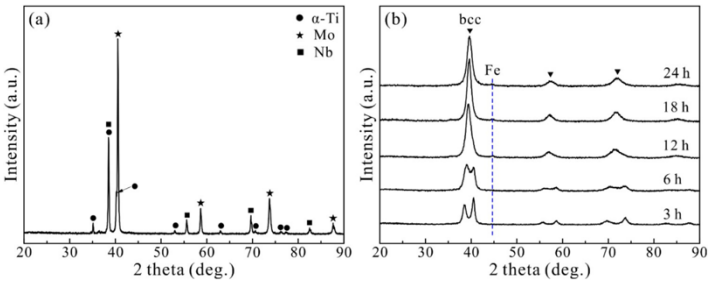
(a)
α-Ti
Mo
Nb
Intensity (a.u.)
2 theta (deg.)
(b)
bcc
Fe
24 h
18 h
12 h
6 h
3 h
Intensity (a.u.)
2 theta (deg.)

Fig 2

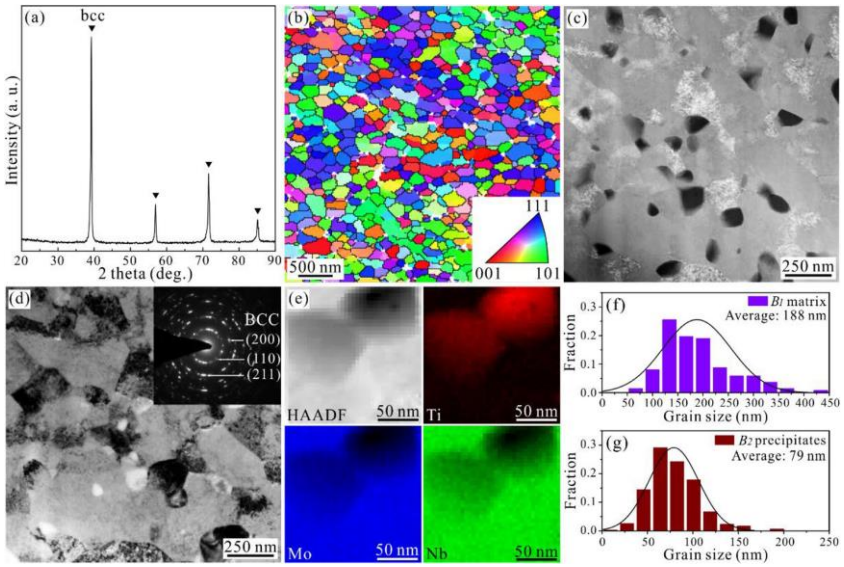
(a)
bcc
Intensity (a. u.)
20 30 40 50 60 70 80 90
2 theta (deg.)
(b)
500 nm
111
001
101
(c)
250 nm
(d)
BCC
(200)
(110)
(211)
250 nm
(e)
HAADF
50 nm
Ti
50 nm
Mo
50 nm
Nb
50 nm
(f)
B1 matrix
Average: 188 nm
Fraction
Grain size (nm)
(g)
B2 precipitates
Average: 79 nm
Fraction
Grain size (nm)

Fig 3

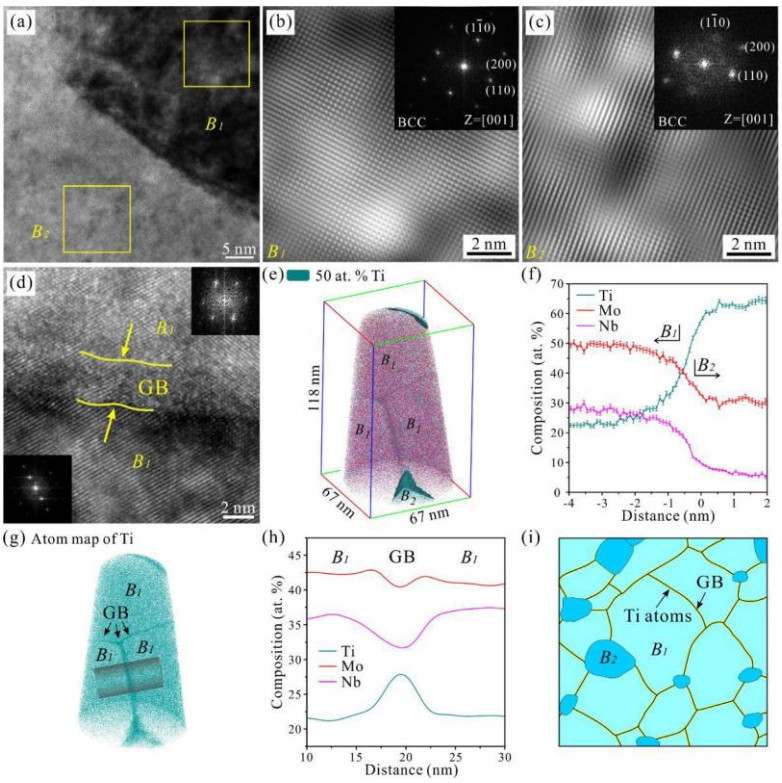
(a)
B1
B2
5 nm
(b)
(1$\bar{1}$0)
(200)
(110)
BCC
Z=[001]
B1
2 nm
(c)
(1$\bar{1}$0)
(200)
(110)
BCC
Z=[001]
B1
2 nm
(d)
B1
GB
B1
2 nm
(e)
50 at. % Ti
118 nm
67 nm
67 nm
B1
B1
B1
B2
(f)
Ti
Mo
Nb
B1
B2
Composition (at. %)
Distance (nm)
(g) Atom map of Ti
B1
GB
B1
B1
(h)
B1
GB
B1
Ti
Mo
Nb
Composition (at. %)
Distance (nm)
(i)
GB
Ti atoms
B2
B1

Fig 4

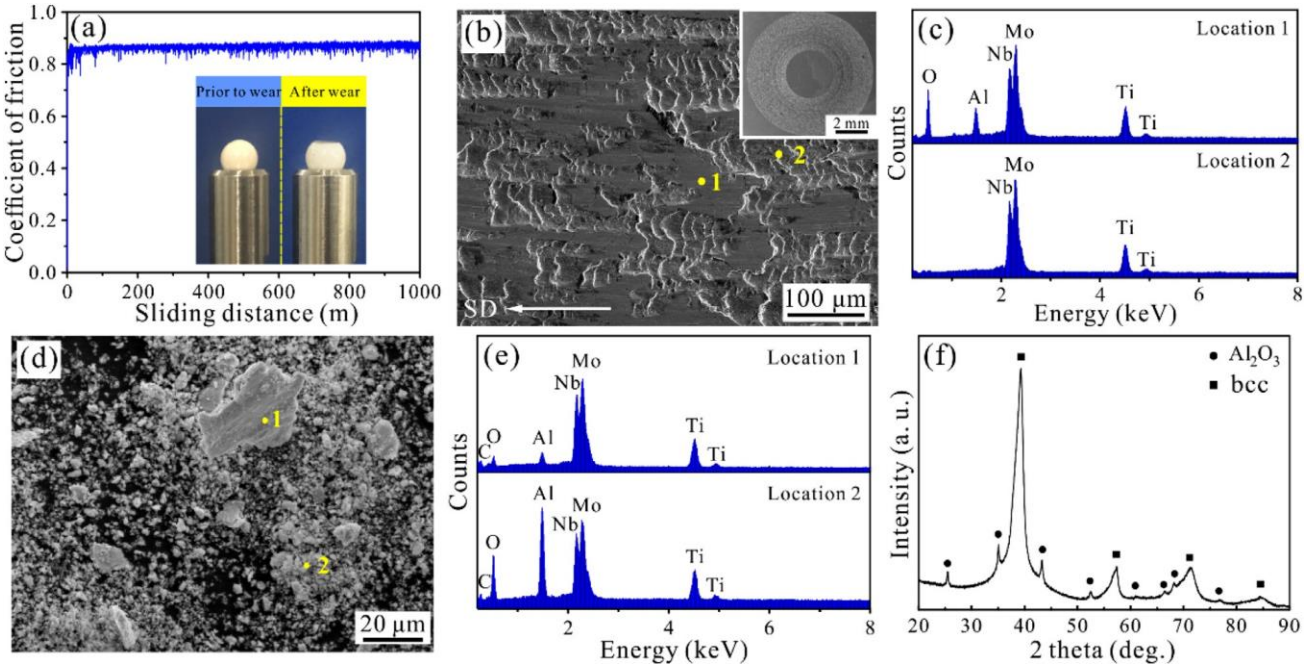
(a)
Coefficient of friction
Sliding distance (m)
Prior to wear
After wear
(b)
SD
100 μm
2 mm
1
2
(c)
Location 1
Location 2
Counts
Energy (keV)
Mo
Nb
O
Al
Ti
(d)
20 μm
(e)
Location 1
Location 2
C
(f)
Al_2O_3
bcc
Intensity (a. u.)
2 theta (deg.)

Fig 5

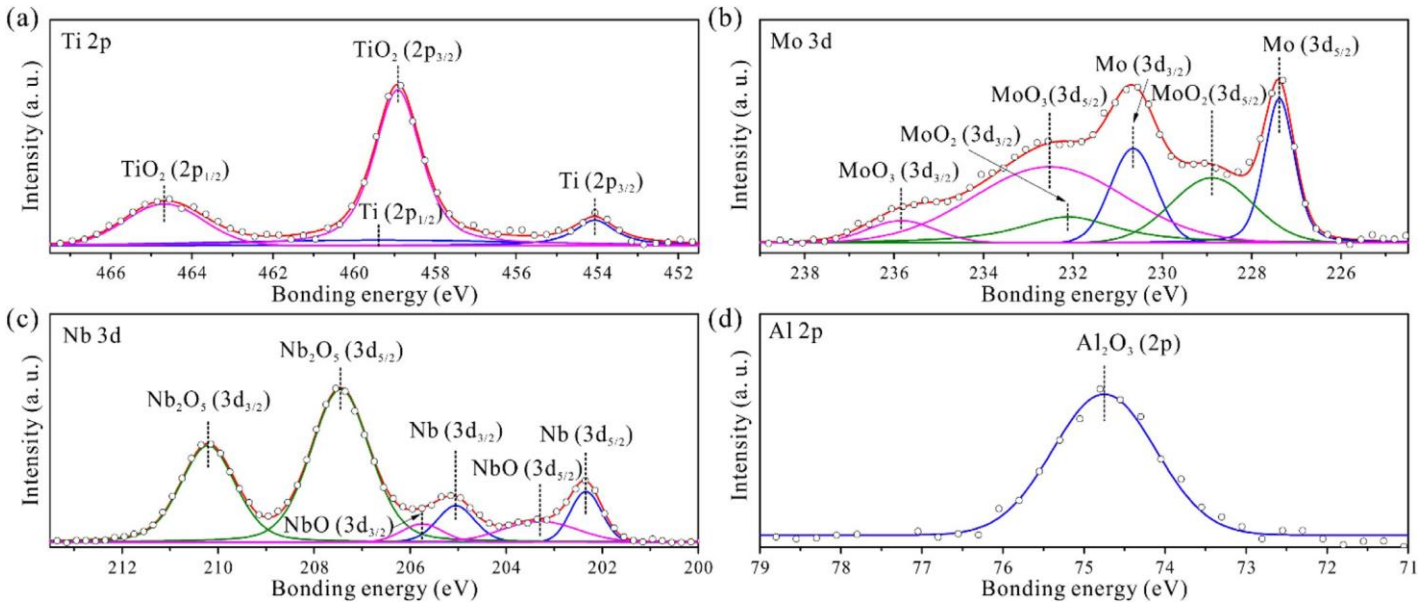
(a)
Ti 2p
TiO2 (2p3/2)
TiO2 (2p1/2)
Ti (2p1/2)
Ti (2p3/2)
Intensity (a. u.)
Bonding energy (eV)
(b)
Mo 3d
Mo (3d3/2)
Mo (3d5/2)
MoO3(3d5/2)
MoO2(3d5/2)
MoO2 (3d3/2)
MoO3 (3d3/2)
Intensity (a. u.)
Bonding energy (eV)
(c)
Nb 3d
Nb2O5 (3d5/2)
Nb2O5 (3d3/2)
Nb (3d3/2)
Nb (3d5/2)
NbO (3d5/2)
NbO (3d3/2)
Intensity (a. u.)
Bonding energy (eV)
(d)
Al 2p
Al2O3 (2p)
Intensity (a. u.)
Bonding energy (eV)

Fig 6

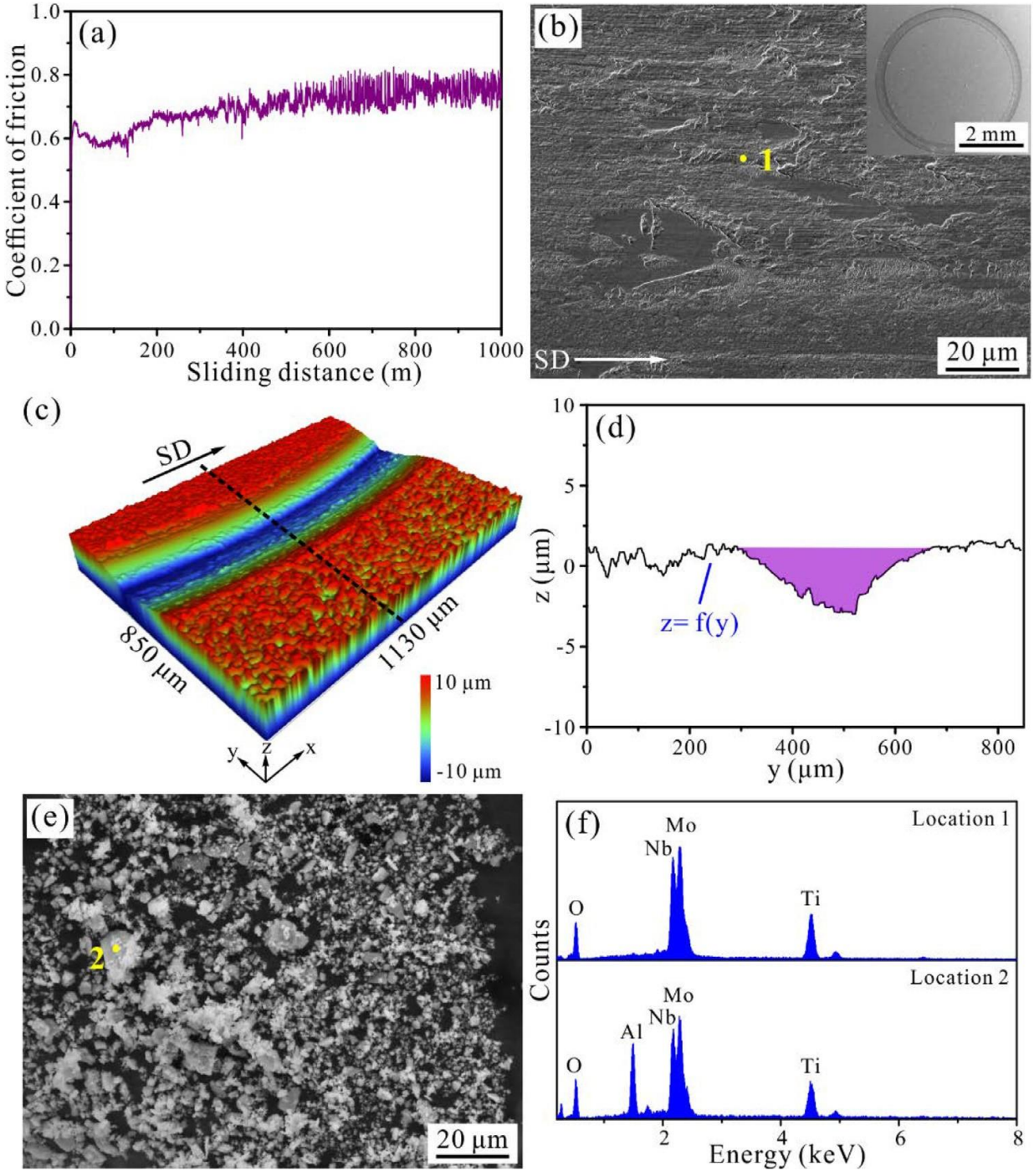
(a)
Coefficient of friction
Sliding distance (m)
(b)
2 mm
1
SD
20 μm
(c)
SD
850 μm
1130 μm
10 μm
-10 μm
y
z
x
(d)
z (μm)
y (μm)
z= f(y)
(e)
2
20 μm
(f)
Location 1
Location 2
Mo
Nb
Ti
O
Al
Counts
Energy (keV)

Fig 7

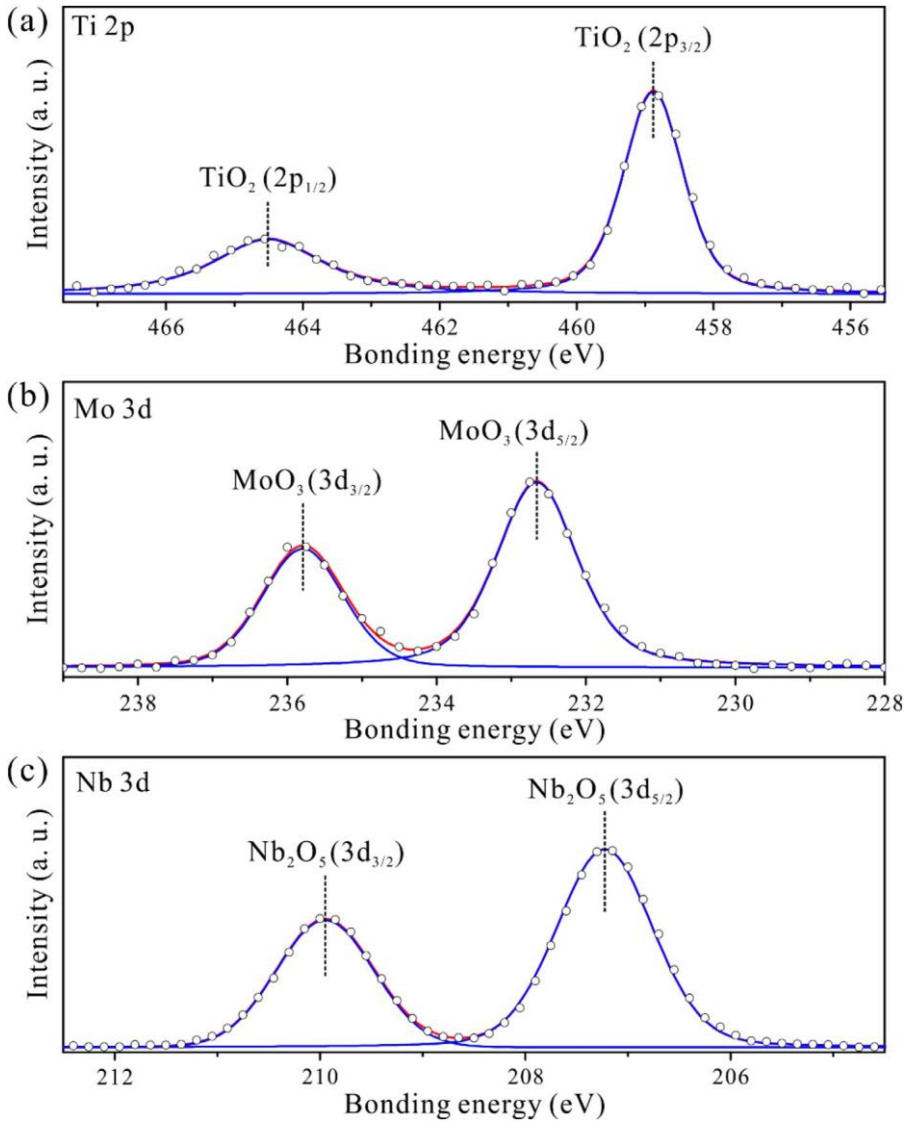
(a)
Ti 2p
TiO_2 ($2p_{3/2}$)
TiO_2 ($2p_{1/2}$)
Intensity (a. u.)
466
464
462
460
458
456
Bonding energy (eV)
(b)
Mo 3d
MoO_3 ($3d_{5/2}$)
MoO_3 ($3d_{3/2}$)
Intensity (a. u.)
238
236
234
232
230
228
Bonding energy (eV)
(c)
Nb 3d
Nb_2O_5 ($3d_{5/2}$)
Nb_2O_5 ($3d_{3/2}$)
Intensity (a. u.)
212
210
208
206
Bonding energy (eV)

Fig 8

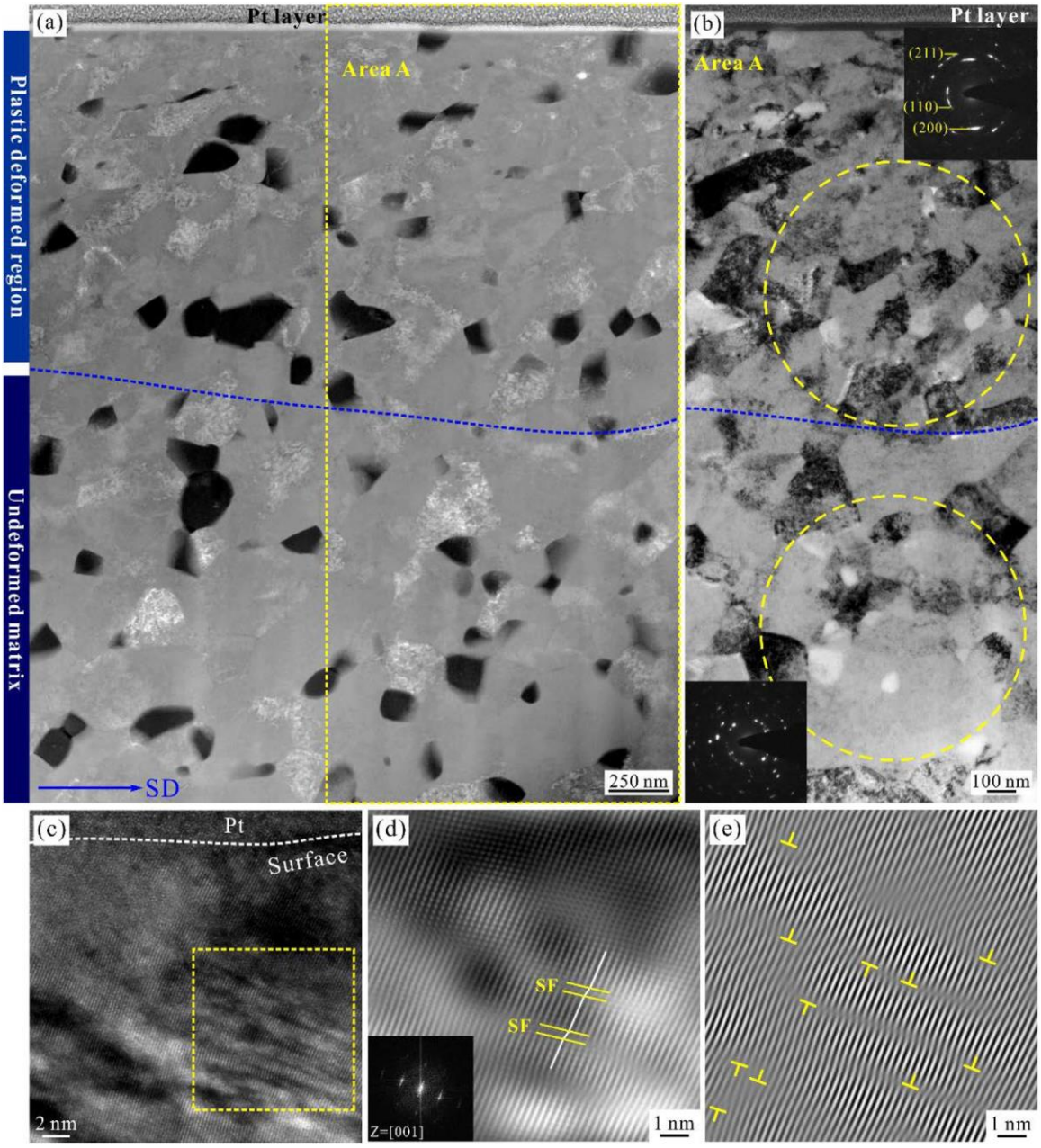
(a)
Pt layer
Area A
Plastic deformed region
Undeformed matrix
SD
250 nm
(b)
Pt layer
Area A
(211)
(110)
(200)
100 nm
(c)
Pt
Surface
2 nm
(d)
SF
SF
Z=[001]
1 nm
(e)
1 nm

Fig 9

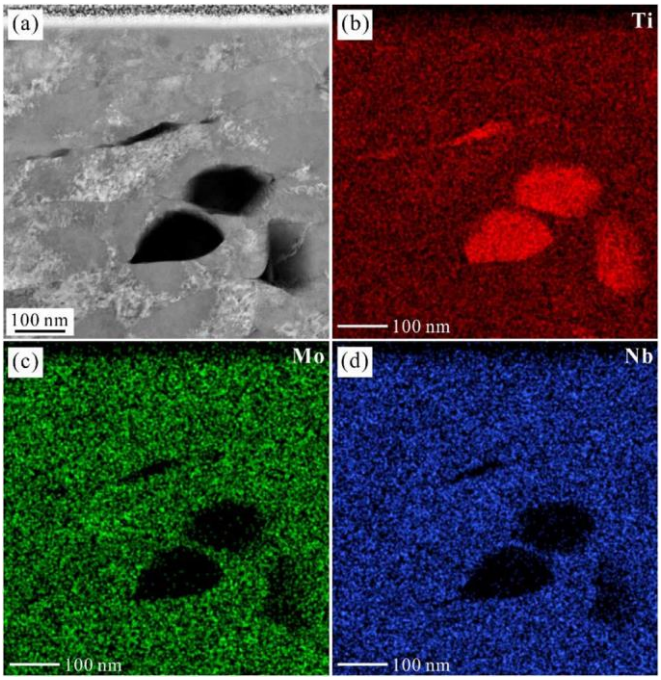

Fig 10

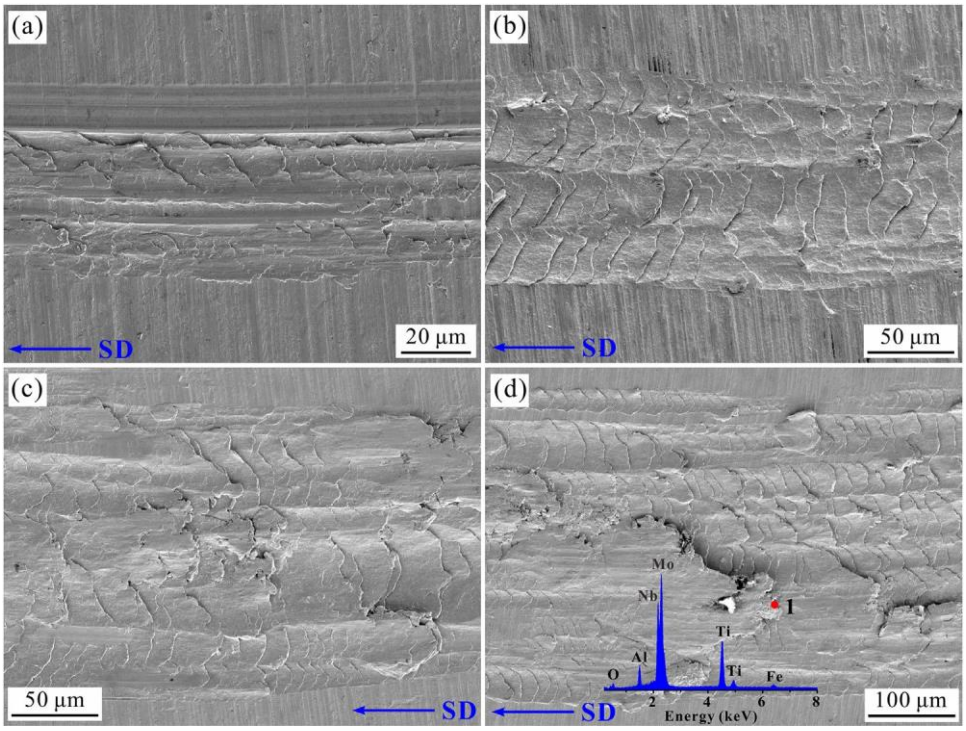
(a)
SD
20 μm
(b)
SD
50 μm
(c)
50 μm
SD
(d)
Mo
Nb
I
Ti
Al
O
Ti
Fe
2
4
6
8
Energy (keV)
SD
100 μm

Fig 11

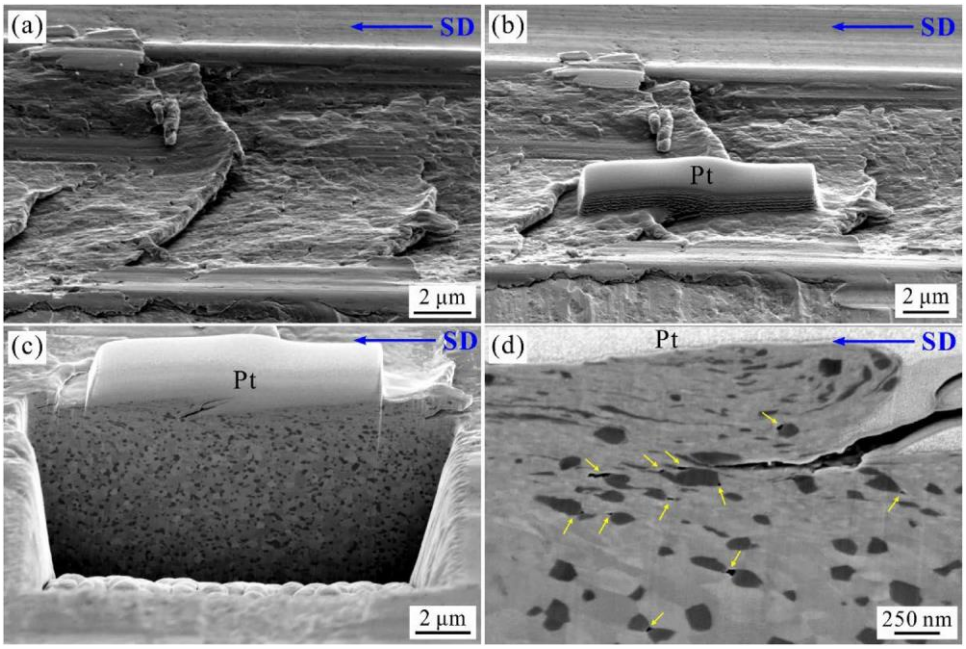

Fig 12

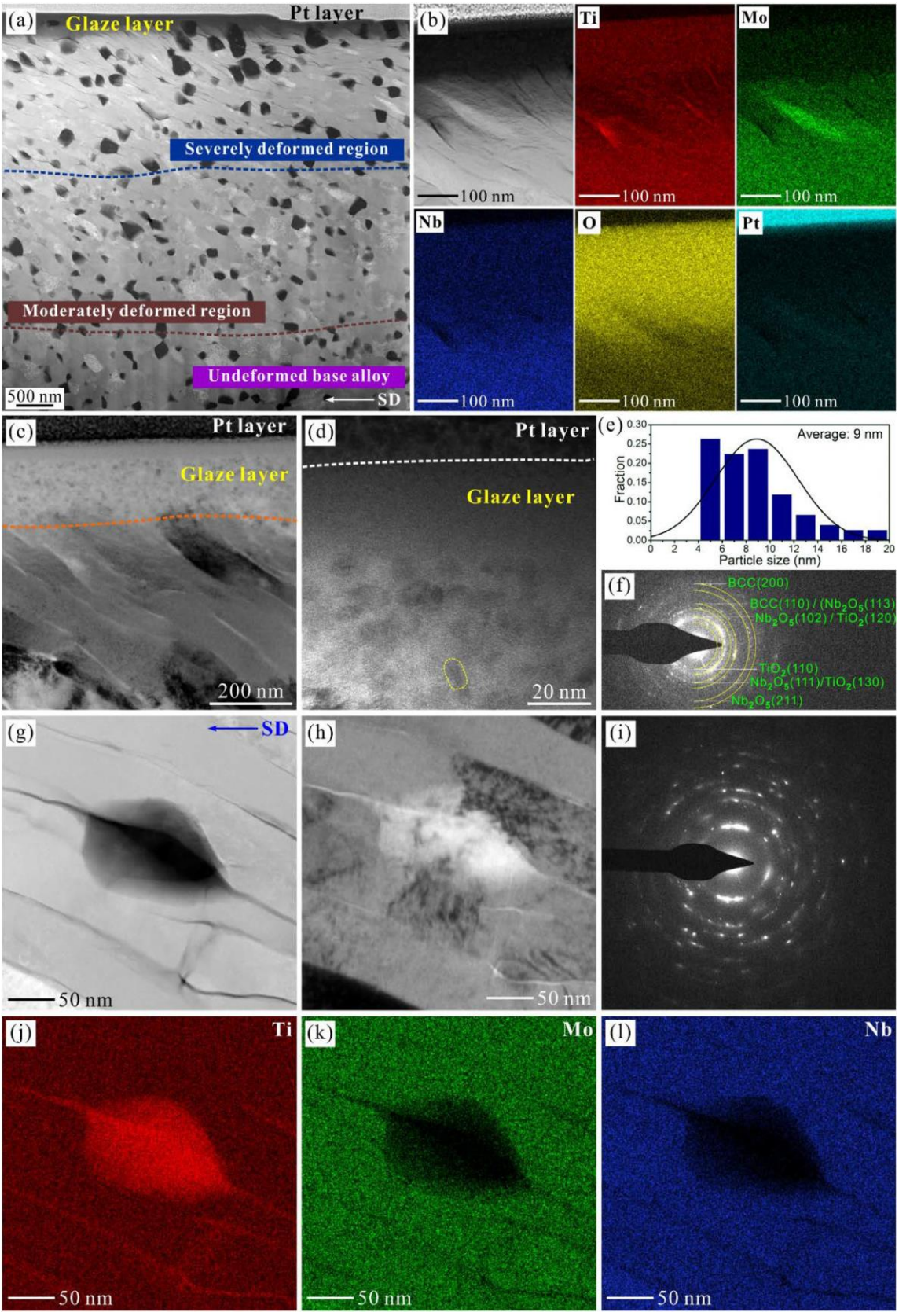
(a)
Glaze layer
Pt layer
Severely deformed region
Moderately deformed region
Undeformed base alloy
500 nm
SD
(b)
100 nm
Ti
Mo
Nb
O
Pt
(c)
Pt layer
Glaze layer
200 nm
(d)
Pt layer
Glaze layer
20 nm
(e)
Average: 9 nm
Fraction
Particle size (nm)
(f)
BCC(200)
BCC(110) / (Nb2O5(113)
Nb2O5(102) / TiO2(120)
TiO2(110)
Nb2O5(111)/TiO2(130)
Nb2O5(211)
(g)
SD
50 nm
(h)
50 nm
(i)
(j)
Ti
50 nm
(k)
Mo
50 nm
(l)
Nb
50 nm

Fig 13

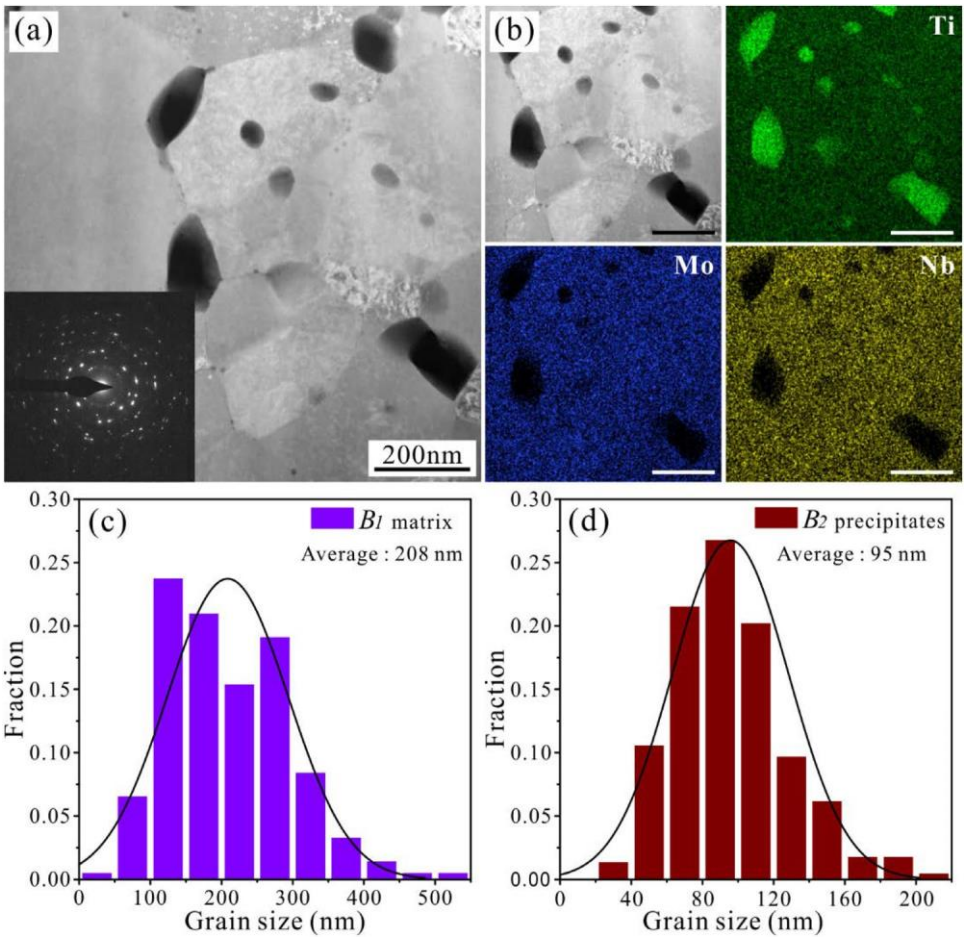
(a)
200nm
(b)
Ti
Mo
Nb
(c)
B1 matrix
Average : 208 nm
Fraction
Grain size (nm)
(d)
B2 precipitates
Average : 95 nm
Fraction
Grain size (nm)